Developments in Earth & Environmental Sciences, 7
Mark O. Barnett and Douglas B. Kent (Editors)

DOI 10.1016/S1571-9197(07)07009-7

Chapter 9

Mechanism of Molybdenum Adsorption on Soils and Soil Minerals Evaluated Using Vibrational Spectroscopy and Surface Complexation Modeling

Sabine Goldberg[1,*], Cliff T. Johnston[2], Donald L. Suarez[1] and Scott M. Lesch[1]

[1]*USDA-ARS, U.S. Salinity Laboratory, 450 W. Big Springs Road, Riverside, CA 92507, USA*
[2]*Crop, Soils, and Environmental Sciences, 915 W. State Street, Purdue University, West Lafayette, IN 47907, USA*

ABSTRACT

Molybdenum adsorption on amorphous aluminum and iron oxides was investigated as a function of solution pH and solution ionic strength. In this study in situ Raman and Fourier transform infrared (FTIR) spectroscopic methods were combined with sorption techniques, electrophoretic mobility measurements, and surface complexation modeling to study the interaction of Mo with amorphous oxide surfaces. The speciation of Mo in aqueous solution was examined using Raman and attenuated total reflectance (ATR)-FTIR methods as a function of solution pH. Good agreement was found between the vibrational spectra of Mo in aqueous solution and those of Mo sorbed to amorphous Al oxide. The mechanisms of Mo sorption to these surfaces based on the spectroscopic, sorption, and electrophoretic mobility measurements are as follows: Mo forms predominantly inner-sphere surface complexes at low pH and predominantly outer-sphere surface complexes at high pH. These surface configurations were used to constrain the input parameters of the triple layer surface complexation model to describe Mo adsorption on soils. After applying the triple layer model to Mo adsorption on 36 soils, a general regression model was developed for predicting Mo surface complexation constants from 5 independently measured soil chemical characteristics: cation exchange capacity, organic carbon content, inorganic carbon

*Corresponding author. Tel.: 951-369-4820; Fax: 951-342-4962;
E-mail: SGOLDBERG@ussl.ars.usda.gov (S. Goldberg).

content, aluminum oxide content, and iron oxide content. The triple layer model was well able to predict Mo adsorption on all the soils at all pH values. The surface speciation predicted by the model for soil was in agreement with that predicted from spectroscopy for Mo adsorption on amorphous Al oxide.

9.1. Introduction

Molybdenum is an essential trace element for both plant and animal nutrition. Molybdenum deficiencies have been reported for many agronomic crops, especially on alkaline soils (Murphy and Walsh, 1972). Molybdenum occurs in anionic form in soil solution, is readily taken up by forage plants, and can accumulate to levels detrimental to grazing ruminant animals (Reisenauer et al., 1973). Molybdenum exerts its toxic effect on ruminants by inducing a copper deficiency that is especially pronounced in the presence of sulfur; this adverse effect can be mitigated by Cu supplementation (O'Connor et al., 2001). At present, our understanding of the biogeochemical factors that influence the bioavailability of Mo is limited. Therefore, careful quantification of soil solution Mo concentration and characterization of Mo adsorption reactions by soil minerals and soils is needed.

Availability of Mo to plants is affected by a variety of soil factors including pH, temperature, texture, clay mineralogy, oxide, and organic matter content (Reisenauer et al., 1973). The active sites that bind Mo are pH dependent sites found on aluminum and iron oxides, clay minerals, and organic matter (Goldberg et al., 1996). Although Mo sorption has been investigated on a wide range of crystalline aluminum (e.g., Ferreiro et al., 1985; Spanos et al., 1990a,b; Vordonis et al., 1990; Spanos and Lycourghiotis, 1995; Goldberg et al., 1996, 1998; El Shafei et al., 2000; Vissenberg et al., 2000) and iron (Kyriacou, 1967; Reyes and Jurinak, 1967; McKenzie, 1983; Ferreiro et al., 1985; Zhang and Sparks, 1989; Goldberg et al., 1996, 1998; Goldberg and Forster, 1998; Lang et al., 2000; Lang and Kaupenjohann, 2003; Xu et al., 2006a,b) oxide minerals, only a few studies have dealt with Mo sorption on amorphous oxides (Jones, 1957; Reisenauer et al., 1962; Bibak and Borggaard, 1994; Goldberg et al., 1996, 1998; Gustafsson, 2003). The features of Mo sorption are consistent with a negatively charged oxyanion in solution where the protonation status of the MoO_4^{2-} and $Mo_7O_{24}^{6-}$ species changes, along with the pH dependent behavior of variable charge sites. Maximum Mo sorption on soils and soil minerals is generally found in the pH range 4–5, and sorption decreases with increasing pH above pH 5 (Gonzalez et al., 1974; Mikkonen and Tummavuori, 1993; Goldberg et al., 1996, 1998).

Descriptions of Mo sorption behavior in natural systems require knowledge of the mode of bonding of the Mo anions on mineral surfaces. Insight into anion adsorption mechanisms can be provided by both macroscopic and microscopic experimental methods. Electrophoretic mobility, for example, measures the movement of charged particles in response to an applied electric field. When anions such as molybdate and phosphate form inner-sphere surface complexes through ligand exchange, the point of zero charge is lowered. The inner-sphere adsorption mechanism was suggested for molybdenum adsorption on crystalline Al and Fe oxides (Ferreiro et al., 1985). Molybdenum adsorption lowered the point of zero charge of crystalline Al and Fe oxides indicating specific adsorption (Goldberg et al., 1996). These shifts in PZC can be used as evidence of strong specific ion adsorption and inner-sphere surface complexation.

Evaluation of the effect of changes in solution ionic strength on the extent of adsorption is another macroscopic method of inferring adsorption mechanisms (Hayes et al., 1988; McBride, 1997). Ions adsorbing as inner-sphere surface complexes show little ionic strength dependence in adsorption behavior. Such was the case for Mo adsorption on goethite (Zhang and Sparks, 1989; Goldberg et al., 1998), gibbsite, and amorphous Fe and Al oxides (Goldberg et al., 1998) suggesting formation of inner-sphere surface complexes.

Investigations of anion desorption reactions have also been used to infer adsorption mechanisms. It was suggested that Mo desorption from goethites was limited due to Mo diffusion into micropores following adsorption (Lang and Kaupenjohann, 2003). Molybdenum desorption from soils was biphasic: the fast reaction was attributed to desorption from Fe oxides and the slow reaction to diffusion out of crystalline oxides (Lang and Kaupenjohann, 1999).

Molybdenum adsorption on soils and soil minerals has been described using various surface complexation modeling approaches: constant capacitance model (Motta and Miranda, 1989; Goldberg et al., 1996, 1998, 2002; Saripalli et al., 2002), diffuse layer model (Dzombak and Morel, 1990; Stollenwerk, 1995; Gustafsson, 2003), triple layer model (Zhang and Sparks, 1989; Goldberg et al., 1998; Wu et al., 2001), and CD-MUSIC model (Bourikas et al., 2001; Gustafsson, 2003; Xu et al., 2006b). The advantage of surface complexation models over empirical adsorption models is that they define specific surface species, chemical reactions, mass balances, and charge balances and contain molecular features that can be given thermodynamic significance (Sposito, 1983).

In a prior study (Goldberg et al., 2002), a general regression model was developed to obtain soil Mo surface complexation constants for use in the

constant capacitance model to predict Mo adsorption. The constant capacitance model parameters were obtained from easily measured soil chemical properties: cation exchange capacity (CEC), organic carbon content (OC), inorganic carbon content (IOC), and free Fe oxide content. The prediction equations, when utilized in the constant capacitance model, provided good prediction of Mo adsorption behavior on 36 soils primarily from California. This comparison of prediction and observation resulted in a completely independent evaluation of the ability of the constant capacitance model to describe Mo adsorption. This approach avoids the necessity of performing time consuming detailed adsorption studies for each specific soil. Predictions of adsorption were obtained using both monodentate and bidentate surface configurations for molybdate and were of similar quality. This is fortunate since no spectroscopic observations have been carried out to date for molybdate adsorption on oxide minerals. Constant capacitance model results underpredicted the experimental Mo adsorption above pH 7.5, thus limiting the use of the model in arid zone soils. It is possible that molybdate forms both inner- and outer-sphere surface complexes on aluminum and iron oxides, as has been observed spectroscopically for the anions, sulfate and selenate (Peak et al., 1999; Wijnja and Schulthess, 2000). Monodentate inner-sphere surface complexes were observed to dominate at pH values below 6 and outer-sphere surface complexes dominated above pH 6–7 for sulfate and selenate adsorption on goethite and aluminum oxide. Simultaneous adsorption as both inner- and outer-sphere surface complexes cannot be described using the constant capacitance model. A three plane model, such as the triple layer model or the CD-MUSIC model, is required.

Our study focuses on molybdate adsorption on amorphous Fe and Al oxides that, unlike crystalline oxides, such as goethite, have not been thoroughly characterized yet, especially with spectroscopic techniques. These materials constitute a major sink for ion adsorption in soils. A combination of macroscopic and microscopic experiments is appropriate to delineate the adsorption mechanism of molybdate. Our study contains the following objectives: (1) to determine Mo adsorption behavior on amorphous Al and Fe oxide as a function of solution pH and ionic strength and PZCs of amorphous Al and Fe oxide with and without molybdate; (2) to evaluate the ability of the triple layer model to describe molybdate adsorption on these oxides and on the soils studied by Goldberg et al. (2002); (3) to develop a set of regression model equations to predict triple layer model parameters and to subsequently predict Mo adsorption on the soils of Goldberg et al. (2002). Our goal was to establish a clear link between the known phase diagram of Mo and the aqueous speciation using Raman and attenuated total reflectance-Fourier transform infrared (ATR-FTIR) methods. In this context,

we were constrained to work at the higher concentrations to make a clear, unambiguous link between the speciation and the spectroscopy.

9.2. Experimental

9.2.1. Macroscopic Experiments

Molybdenum adsorption behavior as a function of solution pH and ionic strength was studied on amorphous Al and Fe oxides synthesized using the method of Sims and Bingham (1968). Iron oxide was synthesized by neutralizing 100 mL of 1.5 M $FeCl_3$ with 225 mL of 2.0 M NaOH. The sample preparation scheme for amorphous Fe oxide used in this paper was that used in Goldberg et al. (1996) and Goldberg (2002). In the Al oxide synthesis, 0.41 M $AlCl_3$ was neutralized with an equal part of 1.1 M NaOH. The sample preparation scheme for amorphous Al oxide used in this paper and Goldberg (2002) was that of Sims and Bingham (1968), while the sample preparation scheme used in Goldberg et al. (1996) was that of McLaughlin et al. (1981). We changed procedures because the Sims and Bingham (1968) method gave much greater yield of solid. X-ray diffraction (XRD) analyses verified that the oxides were amorphous and contained no crystalline impurities detected by XRD. Surface areas (SAs) were determined from a single-point BET N_2 adsorption isotherm. The SA was 65.6 $m^2\,g^{-1}$ for the Al oxide and 169 $m^2\,g^{-1}$ for the Fe oxide.

9.2.1.1. Electrophoretic Mobility

Points of zero charge for the oxides were determined by microelectrophoresis. Electrophoretic mobility measurements of suspensions containing 0.02% oxide in 0.01 M NaCl were determined at various pH values in the presence of 0, 0.01, or 0.1 mM Mo from $Na_2MoO_4 \cdot 2H_2O$. Points of zero charge were obtained by linearly interpolating the data to zero mobility.

9.2.1.2. Adsorption Envelopes

Molybdenum adsorption envelopes (amount of Mo adsorbed as a function of solution pH per fixed total Mo concentration) were determined in batch systems. Samples of 0.1 g of oxide were added to 50 mL polypropylene

centrifuge tubes and equilibrated with 25 mL of a 0.01, 0.1, or 1.0 M NaCl solution by shaking for 20 h on a reciprocating shaker at 23.1 ± 0.1°C. Particle concentration of oxide was 4.0 g L^{-1}. The equilibrating solutions contained 1.0 mM Mo from $Na_2MoO_4 \cdot 2H_2O$ and were adjusted to the desired pH values using 1.0 M HCl or NaOH. The samples were centrifuged and the decantates analyzed for pH, filtered through a 0.45 μm membrane filter, and analyzed for Mo concentration using inductively coupled plasma (ICP) emission spectrometry.

Molybdenum adsorption envelopes on 36 soil samples were determined previously (Goldberg et al., 2002). Physical and chemical characteristics and experimental methods are provided in Goldberg et al. (2002). The soils had the following range of chemical characteristics: pH, 4.1–10.2; CEC, 27–467 $mmol_c\,kg^{-1}$; SA, 21.2–286 $m^2\,g^{-1}$; IOC, 0.001–1.9%; OC, 0.11–3.2%; free Fe oxide (Fe), 0.17–4.9%; and free Al oxide (Al), 0.018–0.37%. Free oxides were determined using the method of Coffin (1963). Free oxides are defined as the oxides and other forms of Fe and Al found in soils but not as a part of the crystal lattice of other minerals present (Coffin, 1963). Molybdenum adsorption envelopes were determined on 5 g of soil equilibrated with 25 mL of a solution containing 0.292 mM Mo from $Na_2MoO_4 \cdot 2H_2O$ for 20 h. All other steps in the adsorption procedure were as listed above for the amorphous oxides.

9.2.2. Vibrational Spectroscopy

9.2.2.1. ATR-FTIR Spectroscopy

FTIR spectra were obtained with a Perkin-Elmer Model 2000/GX spectrometer and a horizontal ATR attachment (Pike Technology®) fitted with a ZnSe internal reflection element with a 45° angle corresponding to nine reflections in contact with the sample. The measured pathlength was 15 μm at 1,630 cm^{-1} based on the molar absorptivity of water. The ZnSe internal reflection element did not permit observation of infrared (IR) bands below 700 cm^{-1}. Spectra were obtained at a resolution of 4 cm^{-1} with each spectrum corresponding to the co-addition of 64 scans using a medium-band liquid N_2 cooled MCT detector. *In situ* ATR-FTIR spectra were obtained by placing 1 mL of an aqueous suspension containing 2 mg of amorphous Al oxide into the ATR cell. The suspension was allowed to dry at room temperature and this resulted in a uniform dry deposit of the oxide on the ZnSe crystal. An aqueous solution of 0.01 M NaCl at pH 8 was then slowly passed over the oxide deposit using the ATR flow through system and a MasterFlex

computerized pump (Cole-Parmer®) and FTIR spectra were recorded. Flow rate of the pump was maintained at 16 mL min^{-1}. Very little oxide was lost during the washing step with NaCl that took a few hours for equilibration. Then Mo was introduced to the flow at a concentration of 0.01 M in a 0.01 M NaCl background electrolyte at pH 8. ATR-FTIR spectra were recorded. The pH of the Mo solution was changed from pH 8 to 3.5 at 0.5 decrements using HCl after recording the spectra at each pH value. Spectra were analyzed using the GRAMS/32 AI® (Version 6.00) program from Galactic software.

9.2.2.2. Raman Spectroscopy

Raman spectra were obtained on an Acton Research Corporation SpectroPro500® spectrograph. A Spectra-Physics Model 127 helium–neon laser with 632.8 nm wavelength and power output of 35 mW measured at the laser head was used as the excitation source. Raman scattered radiation was collected in a 90° scattering configuration. A 1/4 wave plate and polarization analyzer were used to measure Raman depolarization ratios. A calcite-wedge polarization scrambler was placed after the analyzer to minimize unwanted polarization effects in the spectrograph. The polarization discrimination of the instrument was checked by measuring the depolarization ratio for the 459 cm^{-1} band of CCl_4. The experimental value was 0.023 compared to a theoretical value of 0.01. The entrance slits to the spectrograph were set to 100 μm that corresponds to a resolution of 5 cm^{-1}. The spectrograph used a holographic grating with 600 grooves per mm with a blaze wavelength of 532 nm. The detector was a Princeton Instruments liquid N_2 cooled CCD detector with an active array of 1,100 (h) × 330 (v) pixels. The spectrograph was calibrated daily using a Ne–Ar calibration lamp based upon known spectral lines. Spectra were typically collected using 300 s of acquisition on the CCD array. Spectra were analyzed using the GRAMS/32 AI® (Version 6.00) program from Galactic software. Raman spectra of MoO_4 were collected from 0.1 M solutions in 1 cm quartz cuvettes using a 90° backscattering geometry.

9.2.3. Surface Complexation Modeling

A detailed discussion of the theory and assumptions of the triple layer surface complexation model is provided elsewhere (Goldberg, 1992). In the present application of the model to Mo adsorption, the following surface

complexation constants were considered:

$$SOH_{(s)} + H^+_{(aq)} \rightleftarrows SOH^+_{2(s)} \tag{9.1}$$

$$SOH_{(s)} \rightleftarrows SO^-_{(s)} + H^+_{(aq)} \tag{9.2}$$

$$SOH_{(s)} + Na^+_{(aq)} \rightleftarrows SO^- - Na^+_{(s)} + H^+_{(aq)} \tag{9.3}$$

$$SOH_{(s)} + H^+_{(aq)} + Cl^-_{(aq)} \rightleftarrows SOH^+_2 - Cl^-_{(s)} \tag{9.4}$$

$$SOH_{(s)} + H_2MoO_{4(aq)} \rightleftarrows SHMoO_{4(s)} + H_2O \tag{9.5}$$

$$SOH_{(s)} + H_2MoO_{4(aq)} \rightleftarrows SOH^+_2 - HMoO^-_{4(s)} \tag{9.6}$$

or

$$SOH_{(s)} + H_2MoO_{4(aq)} \rightleftarrows SOH^+_2 - MoO^{2-}_{4(s)} + H^+_{(aq)} \tag{9.7}$$

where $SOH_{(s)}$ represents reactive surface hydroxyl groups on oxides and aluminol groups on clay minerals in the soils. Even though the surface complexation reactions are written starting with the completely undissociated acids, the model application contains the aqueous speciation reactions for Mo. Since the quality of model fit to experimental Mo adsorption data on soils was similar for monodentate and bidentate inner-sphere surface species (Goldberg et al., 2002), a monodentate Mo surface configuration was used. A predominantly monodentate surface configuration was found for sulfate adsorption by hematite (Lefevre and Fedoroff, 2006). An outer-sphere complex, Eq. (9.6) or Eq. (9.7), was added in an effort to improve the model fit at pH values above 7 and is consistent with spectroscopic observations for sulfate and selenate adsorption by Al and Fe oxides (Peak et al., 1999; Wijnja and Schulthess, 2000).

Equilibrium constants for the surface complexation reactions are:

$$K_+(\text{int}) = \frac{[SOH^+_2]}{[SOH][H^+]} \exp\left(\frac{F\psi_o}{RT}\right) \tag{9.8}$$

$$K_-(\text{int}) = \frac{[SO^-][H^+]}{[SOH]} \exp\left(-\frac{F\psi_o}{RT}\right) \tag{9.9}$$

$$K_{Na^+}(\text{int}) = \frac{[SO^- - Na^+][H^+]}{[SOH][Na^+]} \exp\left[\frac{F(\psi_\beta - \psi_o)}{RT}\right] \tag{9.10}$$

$$K_{Cl^-}(\text{int}) = \frac{[SOH_2^+ - Cl^-]}{[SOH][H^+][Cl^-]} \exp\left[\frac{F(\psi_o - \psi_\beta)}{RT}\right] \tag{9.11}$$

$$K_{Mo}^{is}(\text{int}) = \frac{[SHMoO_4]}{[SOH][H_2MoO_4]} \tag{9.12}$$

$$K_{Mo}^{1os}(\text{int}) = \frac{[SOH_2^+ - HMoO_4^-]}{[SOH][H_2MoO_4]} \exp\left[\frac{F(\psi_o - \psi_\beta)}{RT}\right] \tag{9.13}$$

or

$$K_{Mo}^{2os}(\text{int}) = \frac{[SOH_2^+ - MoO_4^{2-}]}{[SOH][H_2MoO_4]} \exp\left[\frac{F(\psi_o - 2\psi_\beta)}{RT}\right] \tag{9.14}$$

where F is the Faraday constant ($C\,mol_c^{-1}$), ψ the surface potential (V), R the molar gas constant ($J\,mol^{-1}\,K^{-1}$), T the absolute temperature (K), and square brackets indicate concentrations ($mol\,L^{-1}$). The exponential terms can be considered as solid-phase activity coefficients correcting for charge on the surface complexes.

Mass balance of the surface functional group is:

$$[SOH]_T = [SOH] + [SOH_2^+] + [SO^-] + [SO^- - Na^+] + [SOH_2^+ - Cl^-] + [SHMoO_4] + [SOH_2^+ - HMoO_4^-] \text{ or } + [SOH_2^+ - MoO_4^{2-}] \tag{9.15}$$

and the charge balances are:

$$\sigma_o + \sigma_\beta + \sigma_d = 0 \tag{9.16}$$

$$\sigma_o = [SOH_2^+] + [SOH_2^+ - Cl^-] - [SO^-] - [SO^- - Na^+] + [SOH_2^+ - HMoO_4^-] \text{ or } + [SOH_2^+ - MoO_4^{2-}] \tag{9.17}$$

$$\sigma_\beta = [SO^- - Na^+] - [SOH_2^+ - Cl^-] - [SOH_2^+ - HMoO_4^-] \text{ or } - 2\,[SOH_2^+ - MoO_4^{2-}] \tag{9.18}$$

where σ_i has units of ($mol_c\,L^{-1}$).

The computer code FITEQL 3.2 (Herbelin and Westall, 1996) was used to fit the Mo surface complexation constants to the experimental Mo adsorption data. The FITEQL program uses a nonlinear least squares optimization routine to fit equilibrium constants to experimental data and contains the triple layer model of adsorption. It can also be used as a chemical speciation program to evaluate predictions of Mo adsorption, such as those obtained using the regression model of Goldberg et al. (2002) to predict values of the Mo surface complexation constant from soil chemical properties.

In our application of the triple layer model, the surface site density was fixed at a value of 2.31 sites nm^{-2}, as recommended by Davis and Kent (1990) for natural materials. Numerical values for the protonation constant, the dissociation constant, and the surface complexation constants for the background electrolyte were obtained from the literature. For the amorphous Al oxide and the soils we used $\log K_+(\text{int}) = 5.0$, $\log K_-(\text{int}) = -11.2$, $\log K_{Na+}(\text{int}) = -8.6$, and $\log K_{Cl-}(\text{int}) = 7.5$ obtained by Sprycha (1989a,b) for γ-Al_2O_3. For the amorphous Fe oxide we used $\log K_+(\text{int}) = 4.3$, $\log K_-(\text{int}) = -9.8$, $\log K_{Na+}(\text{int}) = -9.3$, and $\log K_{Cl-}(\text{int}) = 5.4$ obtained by Zhang and Sparks (1990) for goethite. We used parameter values for crystalline oxides since values for amorphous oxides were not available. Molybdate surface complexation constants were fit simultaneously to the oxide adsorption data at three different ionic strengths using the inner-sphere, Eq. (9.5), and an outer-sphere, Eq. (9.6) or Eq. (9.7), adsorption mechanism. The capacitance values were fixed at $C_1 = 1.2\,F\,m^{-2}$ and $C_2 = 0.2\,F\,m^{-2}$ considered optimal for goethite by Zhang and Sparks (1990). When developing data bases of surface complexation constants, it is critically important to use consistent values of surface site density, capacitances, protonation-dissociation constants, and background electrolyte surface complexation constants. Constant values of these parameters are necessary to allow application of predictive equations to new soils.

9.3. Results and Discussion

9.3.1. Macroscopic Experiments

9.3.1.1. Electrophoretic Mobility

Points of zero charge occurred at pH 7.8 for amorphous Fe oxide and at pH 9.4 for amorphous Al oxide. These PZCs are in excellent agreement with numerous literature values. Figure 9.1 presents electrophoretic mobility versus pH obtained upon adsorption of Mo onto amorphous Fe oxide (Fig. 9.1a) and amorphous Al oxide (Fig. 9.1b). The PZCs were shifted to lower pH value with increasing Mo concentration, characteristic of inner-sphere adsorption. This is clearly seen for the amorphous Fe oxide in the presence of Mo (Fig. 9.1a). The PZC of amorphous Al oxide decreased only slightly in the presence of increasing Mo concentrations (Fig. 9.1b) indicating the predominance of either an outer-sphere Mo surface complex, an inner-sphere Mo surface complex that did not change the surface charge, or a

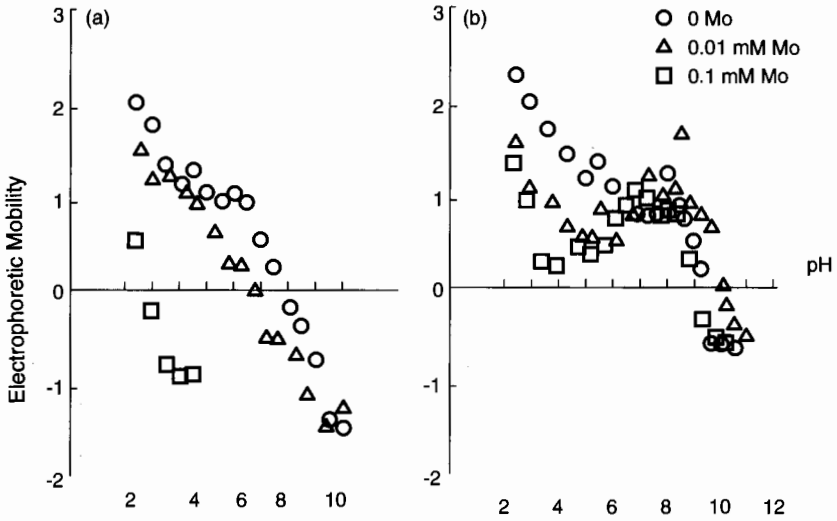

Figure 9.1: Electrophoretic Mobility of Amorphous Oxides as a Function of pH and Total Mo Concentration in 0.01 M NaCl Solution: (a) Fe Oxide; (b) Al Oxide. Circles Represent the Zero Mo Treatment.

combination of both of these surface complexes. It is possible that the strange local maxima and minima in the Al oxide system are due to the predominance of inner-sphere Mo surface complexes at low pH and the predominance of outer-sphere Mo surface complexes at higher pH.

9.3.1.2. Adsorption Envelopes

The effect of ionic strength on Mo adsorption on amorphous Al and Fe oxides is indicated in Fig. 9.2. Solution ionic strength varied by two orders of magnitude, from 0.01 to 1.0 M NaCl. Molybdate adsorption on amorphous oxides decreased with increasing solution pH. On amorphous Fe oxide, Mo adsorption exhibited no ionic strength dependence with increasing solution ionic strength (Fig. 9.2a). This behavior is indicative of an inner-sphere adsorption mechanism, in agreement with the mechanism inferred from PZC shift results for this material. On amorphous Al oxide, Mo adsorption exhibited decreasing adsorption with increasing ionic strength (Fig. 9.2b), indicative of an outer-sphere adsorption mechanism. This result is in agreement with the PZC shift results, which suggest that the majority of Mo adsorption may be outer-sphere. Our results indicate that Mo is more tightly

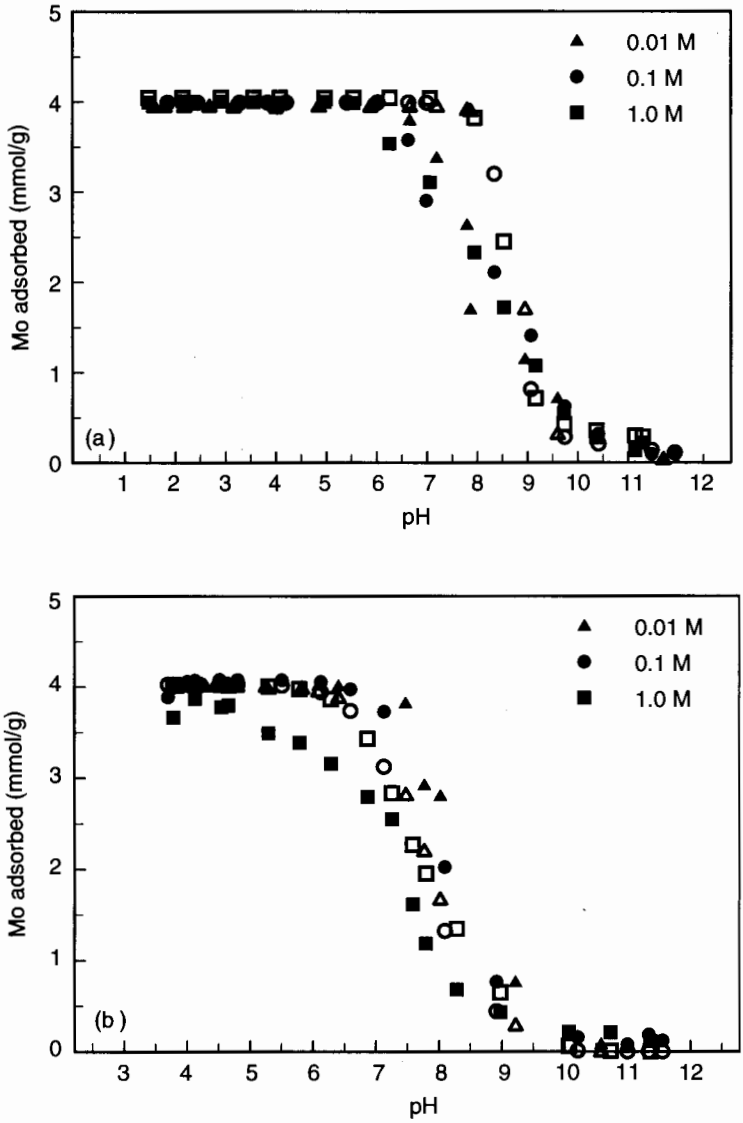

Figure 9.2: Fit of the Triple Layer Model to Mo Adsorption on Amorphous Oxides as a Function of Solution pH and Ionic Strength: (a) Fe Oxide; (b) Al Oxide. Particle Concentration = 4.0 g L^{-1}. Solid Symbols Represent Experimental Data Points. Open Symbols Represent Model Fits using an Inner-Sphere and an Outer-Sphere Mo Surface Complex. Log K^{is}_{Mo}(int) = 12.43, log K^{2os}_{Mo}(int) = 3.76 for Fe Oxide. Log K^{is}_{Mo}(int) = 10.55, log K^{1os}_{Mo}(int) = 12.58 for Al Oxide.

bound to Fe oxide than to Al oxide, similar to our previous observations for arsenite adsorption on amorphous oxides (Goldberg and Johnston, 2001).

9.3.2. Vibrational Spectroscopy

The ATR-FTIR spectra of a 2 mg deposit of amorphous Al oxide deposit on a ZnSe internal reflection element in the presence of 10 mM NaCl at pH 8 are shown in Fig. 9.3 (represented by a dashed line). The predominant band is found at 973 cm^{-1} and weaker bands at 1,419 and 1,497 cm^{-1}. The 973 cm^{-1} band corresponds to the Al–O–H bending vibration (Farmer, 1974; Wang and Johnston, 2000). The bands at 1,419 and 1,497 cm^{-1} correspond to the v_3 asymmetric stretch of sorbed carbonate (Su and Suarez, 1997). Since the PZC of this amorphous Al oxide is 9.4, it will have a net positive surface charge and attract aqueous carbonate species in solution at all pH values

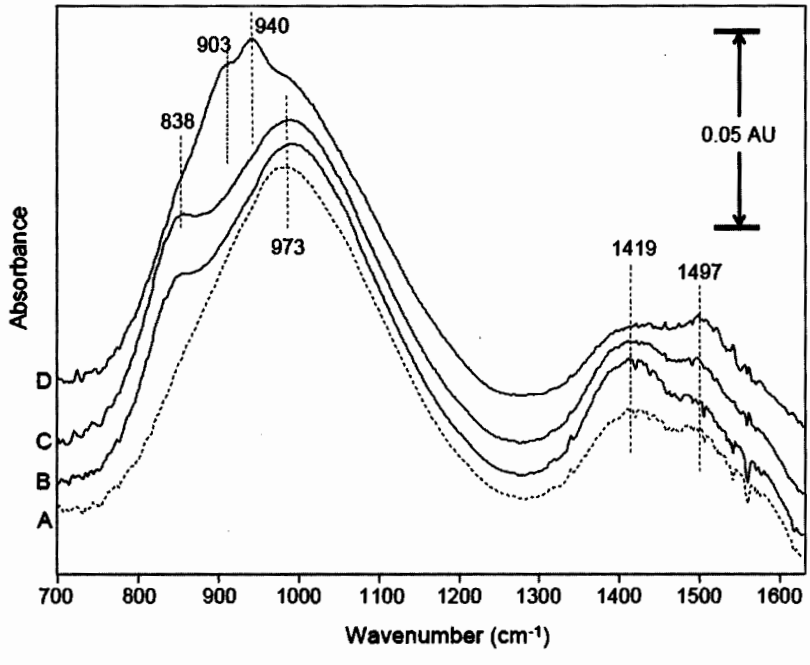

Figure 9.3: ATR-FTIR Spectra of a 2 mg Deposit of Amorphous Al Oxide in a 10 mM NaCl Solution on a ZnSe Internal Reflection Element: (A) 10 mM NaCl Solution at pH 8; (B) 10 mM NaCl Solution and 10 mM Mo Solution at pH 8; (C) 10 mM NaCl and 10 mM Mo Solution at pH 6; (D) 10 mM NaCl and 10 mM Mo Solution at pH 4.

used in this study. Molybdate was introduced into the ATR-FTIR cell as a 10 mM $NaHMoO_4$ solution with a background electrolyte concentration of 10 mM NaCl adjusted to pH 8 using a peristaltic pump at a flow rate of 16 mLmin^{-1}. Based on prior work, aqueous molybdate species are known to interact with amorphous Al oxide to a greater extent at low pH (Goldberg et al., 1996). Thus, the experiment was started at pH 8 and the pH was lowered in 0.5 pH unit decrements until a pH value of 3.5 was reached. The ATR-FTIR spectrum of the Mo–Al oxide complex at pH 8 is shown as Spectrum B in Fig. 9.3. The presence of sorbed MoO_4 is revealed by the shoulder at 838 cm^{-1}. The carbonate bands at 1,419 and 1,497 cm^{-1} are more distinct at this high pH value indicating the presence of sorbed carbonate. The spectra of sorbed Mo did not change significantly until the pH of the aqueous solution was decreased to <6 where "new" bands at 903 and 940 cm^{-1} appeared (Spectra C and D in Fig. 9.3 were obtained at pH values of 6 and 4, respectively).

To observe the spectral changes induced by Mo sorption, difference spectra were obtained by subtracting the ATR-FTIR spectrum of the amorphous Al oxide deposit from the spectra of the Mo–Al oxide complexes (Fig. 9.4). In this case, Spectrum A (Fig. 9.3) was subtracted from the Mo–Al oxide complexes. For example, the difference spectrum at pH 8 was obtained by subtracting Spectrum A from Spectrum B (Fig. 9.3). At pH 8, the difference spectrum clearly shows the presence of the sorbed Mo species by the bands at 838 and 1,020 cm^{-1}. Upon lowering the pH, two new bands appear at 903 and 940 cm^{-1}, with a concomitant decrease in the intensities of the bands at 838 and 1,020 cm^{-1}. The spectrum of the amorphous Al oxide did not change shape upon lowering the pH. The ATR-FTIR spectrum of the amorphous Al oxide deposited on the ATR cell at pH 8 (prior to the addition of Mo) was used as the reference file for all spectral subtractions. The observed Mo bands are not due to changes in bandshape of the Al oxide itself. Confirmation of this is found in the agreement of the Mo bands sorbed to the Al oxide surface with the spectra of Mo in aqueous solution.

To better understand the solution speciation of Mo, ATR-FTIR and Raman spectra of aqueous Mo species were obtained as a function of pH and ionic strength and are shown in Fig. 9.5. The ATR-FTIR spectra of a 100 mM aqueous Mo solution in 10 mM NaCl are shown in Fig. 9.5a. The solution ATR-FTIR spectra show similar trends to the spectra of sorbed Mo: a strong feature at 837 cm^{-1} along with a weak, broad band at 1,015 cm^{-1} at pH 8–9 that "transitions" into bands at 904 and 941 cm^{-1} at pH values <6 (Weinstock et al., 1973; Jeziorowski and Knozinger, 1979; Tossell, 2005). Raman spectra provide complimentary speciation information because the selection rules that govern Raman- and IR-allowed

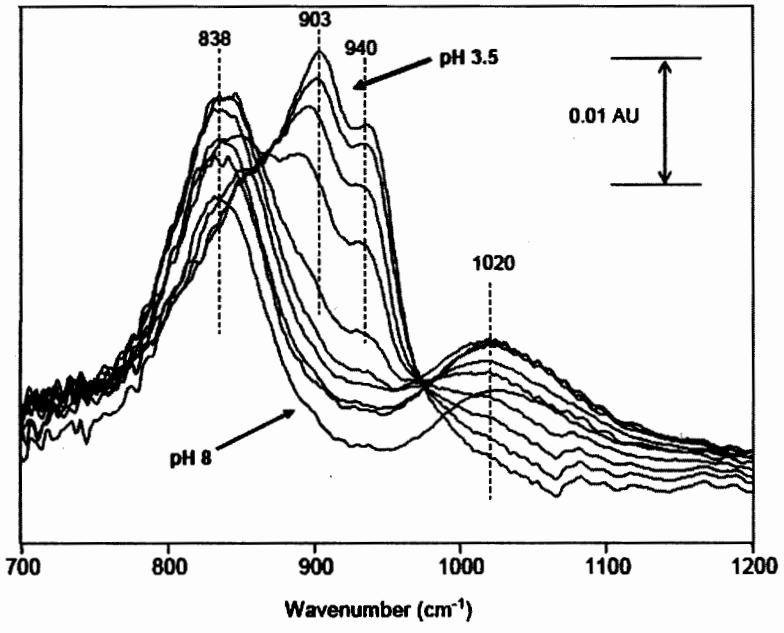

Figure 9.4: ATR-FTIR Difference Spectra of 10 mM Mo in 10 mM NaCl Sorbed to Al Oxide (the Difference Spectra shown here were Obtained from the Spectra shown in Fig. 9.3). Difference Spectra were Obtained by Subtracting the ATR-FTIR Spectrum of the Al Oxide Deposit in 10 mM NaCl at pH 8 from Each of the Spectra shown in Fig. 9.3.

vibrational transitions are different (Herzberg, 1945; Long, 1977; Johnston and Aochi, 1996; Johnston and Wang, 2002). In the Raman spectra of the aqueous Mo species, the high pH (pH 8–9) spectra are dominated by a medium intensity band at 837 cm^{-1} and a sharp, well-resolved band at 897 cm^{-1} (Fig. 9.5b). The Raman spectra are strongly influenced by pH with the 837 and 897 cm^{-1} bands diminishing in intensity with "new" bands appearing at 946 and 961 cm^{-1}.

The aqueous speciation of Mo is shown in the inset of Fig. 9.5. At a concentration of 100 mM and at pH value > ~5.8, the dominant species in solution is MoO_4^{2-}. Upon lowering the pH below 5.8, the polymer $Mo_7O_{24}^{6-}$ becomes the predominant species in the narrow pH range of ~5.8 to 5.5. The singly-protonated $HMo_7O_{24}^{5-}$ species dominates from pH 5.5 to 4.2, with the doubly-protonated $H_2Mo_7O_{24}^{4-}$ species present at pH values < 4.2.

Figure 9.6 shows the comparison of the ATR-FTIR spectrum of Mo sorbed to Al oxide at pH 8 (Spectrum C) to the Raman (Spectrum A) and ATR-FTIR (Spectrum B) spectra of a 100 mM Mo solution at pH 8. There is

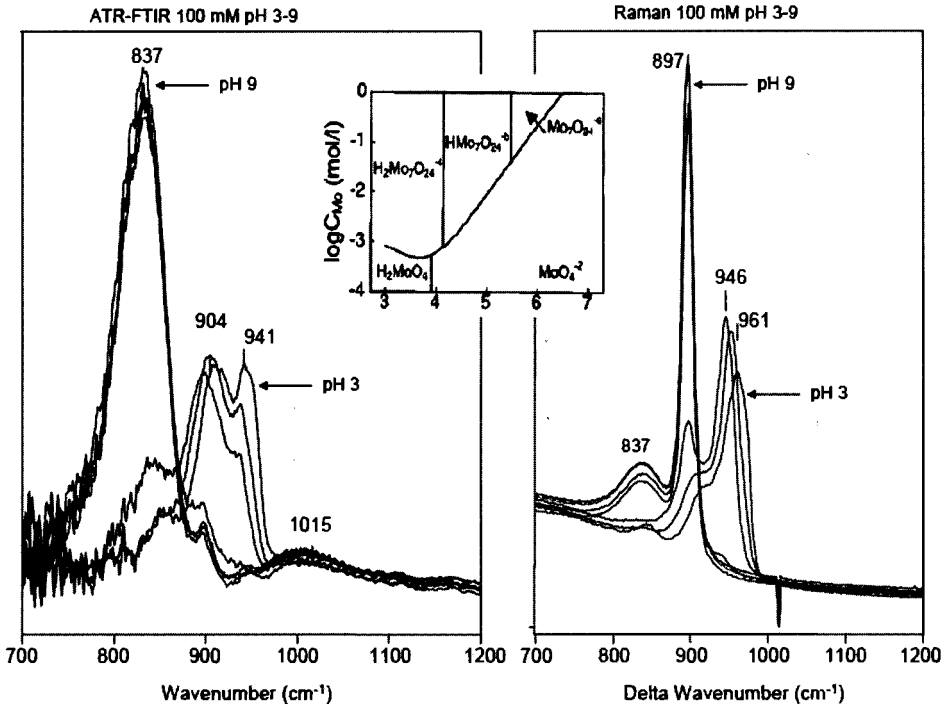

Figure 9.5: (a) ATR-FTIR Spectra of 100 mM Mo in Aqueous Solution as a Function of pH between pH 3 and 9 Plotted in the Region from 700 to 1,200 cm^{-1}, (b) Raman Spectra of 100 mM Mo in Aqueous Solution as a Function of pH between pH 3 and 9 in the Region from 700 to 1,200 cm^{-1}. Inset is from Bourikas et al. (2001).

good agreement between the ATR-FTIR spectra of Mo sorbed to Al oxide (Spectrum C) with that of the ATR-FTIR spectrum of Mo in aqueous solution at pH 8 (Spectrum B). According to the speciation diagram (Fig. 9.5, inset), the dominant solution species is MoO_4^{2-}, consistent with the observed spectra. It is interesting to note that the 1,015 cm^{-1} band is stronger when Mo is sorbed to the Al oxide surface. The corresponding spectra of Mo sorbed to Al oxide at pH 4 and the solution Raman and ATR-FTIR spectra of aqueous Mo at pH 4 are shown in Fig. 9.7. The ATR-FTIR spectrum of Mo sorbed to Al oxide at pH 4 (Spectrum C; Fig. 9.7) is characterized by three bands at 845, 903, and 940 cm^{-1}. The solution Raman (Spectrum A) and ATR-FTIR (Spectrum B) spectra of Mo in aqueous solution have essentially no intensity at 845 cm^{-1} and are characterized by bands at 903 and 940–952 cm^{-1}.

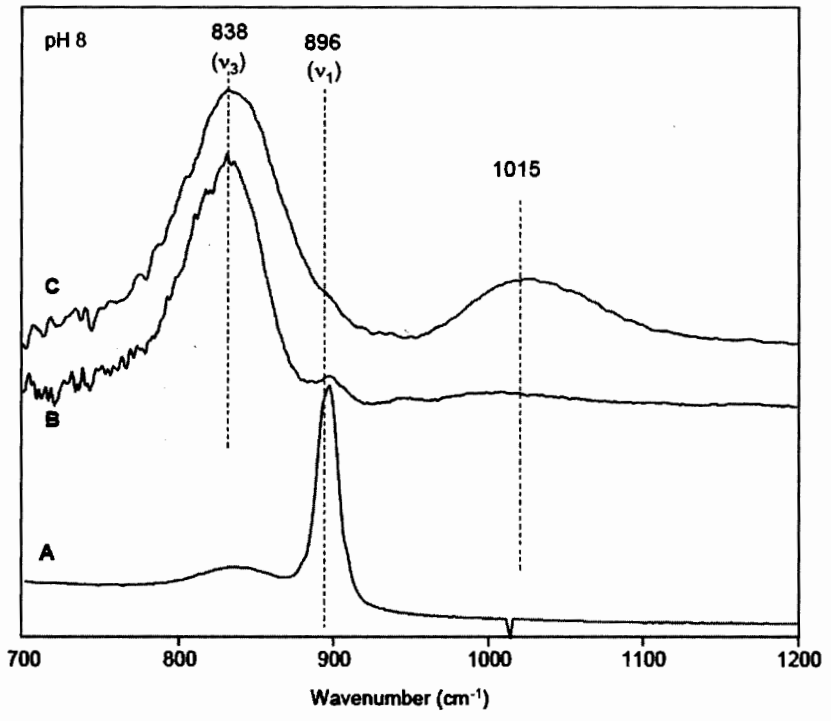

Figure 9.6: Spectrum A Corresponds to the Raman Spectrum of a 100 mM Mo Solution at pH 8 in the 700–1,200 cm^{-1} Region. Spectrum B was Obtained from the Same Solution as for Spectrum A using a 9-bounce ATR-FTIR Solution Cell with a ZnSe IRE. Spectrum C Corresponds to the Difference ATR-FTIR Spectrum of a 10 mM Mo Solution Sorbed to Al Oxide at pH 8.

To the best of our knowledge, a detailed spectroscopic understanding of Mo speciation in aqueous media is not currently known. Based on recent experimental and theoretical work, however, the following conclusions can be drawn from the literature. At pH values > 6, the dominant Mo species in aqueous solution is MoO_4^{2-} (Bourikas et al., 2001). This species is characterized by Raman-active bands at 894, 837, and 318 cm^{-1} (Weinstock et al., 1973). The band at 894 cm^{-1} has been assigned to the ν_1 (a_1) symmetric stretch, the band at 837 cm^{-1} to the ν_3 (t_2) asymmetric stretch, and the 318 cm^{-1} band to the ν_4 (t_2) bend. This is consistent with the bands we observed in the Raman spectrum of Mo at pH 9 (Fig. 9.5b). The symmetric Mo–O stretch has very high intensity in the Raman spectrum, whereas the asymmetric stretch has greater intensity in the FTIR spectrum, consistent

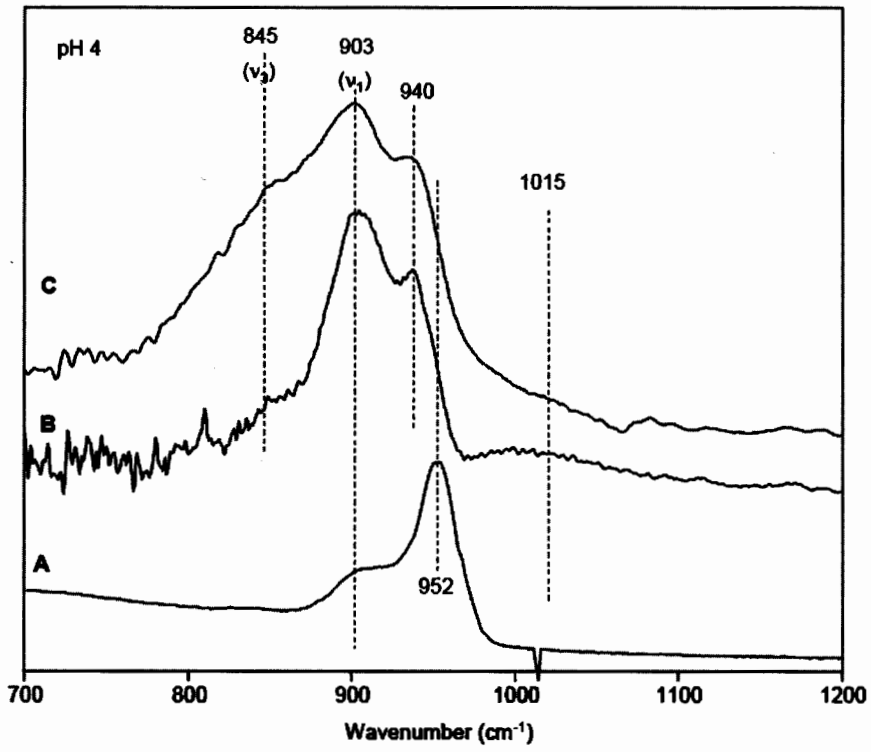

Figure 9.7: Spectrum A Corresponds to the Raman Spectrum of a 100 mM Mo Solution at pH 4 in the 700–1,200 cm^{-1} Region. Spectrum B was Obtained from the Same Solution as for Spectrum A using a 9-bounce ATR-FTIR Solution Cell with a ZnSe IRE. Spectrum C Corresponds to the Difference ATR-FTIR Spectrum of a 10 mM Mo Solution Sorbed to Al Oxide at pH 4.

with the selection rules. We also observed the depolarization ratio of the 897 cm^{-1} band to be very low (~0.02, not shown), confirming the assignment of the 897 cm^{-1} band to the symmetric Mo–O stretch (Long, 1977). Only highly symmetric vibrations, such as the symmetric stretch of an XY_4 molecule have very low depolarization ratios. In a related study (Goldberg and Johnston, 2001), we found similar results for the symmetric As–O stretch of the AsO_4^{3-} species. Jeziorowski and Knozinger (1979) reported Raman spectra of MoO_4^{2-} (pH 11) and $Mo_7O_{24}^{6-}$ (pH 6), but did not indicate the concentration of the Mo species in solution. According to a more recent speciation study (Bourikas et al., 2001), the distribution of MoO_4^{2-} and $Mo_7O_{24}^{6-}$ would be present at approximately the same concentrations, so that

the Raman spectra collected at pH 6 would most likely contain contributions from both species.

Upon decreasing the pH of the aqueous Mo solution to pH values < 6, the 837 and 897 cm^{-1} bands diminish in intensity and "new" bands appear at 903 (R + IR active), 940 (IR active), and 952 (R active) cm^{-1} (see Fig. 9.7). These bands have been assigned to the formation of a polymeric $Mo_7O_{24}^{6-}$ species in aqueous solution. At pH values > 6, the speciation is dominated by the MoO_4^{2-} species where Mo is in tetrahedral coordination. In contrast, the $Mo_7O_{24}^{6-}$ complex is made up of MoO_6 octahedra (Knozinger and Jeziorowski, 1978; Jeziorowski and Knozinger, 1979). Thus, the spectral changes that occur upon lowering the pH are due to: (i) the formation of a polymeric species and (ii) the transition of Mo from a tetrahedrally coordinated species to an octahedrally coordinated species. More recently, there have been several matrix-isolation FTIR studies where Mo species were deposited on a cold window (10 K) in an inert gas matrix (e.g., Ar) (Bare et al., 1998; Wang and Andrews, 2006). This technique provides a very powerful tool for examining Mo species under very carefully controlled conditions. In our case, however, it is difficult to make a direct comparison between our observed Raman and ATR-FTIR spectra and matrix-isolated FTIR spectra of Mo species because our spectra, obtained in aqueous media/suspensions, are often dominated by intermolecular interactions with water.

Although the $Mo_7O_{24}^{6-}$ species is the dominant form of Mo in aqueous solution at pH values < 6, Jeziorowski and Knozinger (1979) attributed sorption of Mo by alumina to the formation of an inner-sphere complex with MoO_4^{2-}. Possible surface complexes of Mo sorbed to alumina catalysts included a bidentate surface complex and a two-dimensional polymeric surface species (Jeziorowski and Knozinger, 1979). It is important to note that all of the Mo surface species considered involve the formation of inner-sphere surface complexes.

Based on the literature and our spectroscopic observations, we draw the following conclusions. At high pH, we have excellent agreement between the observed solution ATR-FTIR spectra and those of Mo sorbed to the amorphous Al oxide in aqueous suspension. We assign the 838 cm^{-1} band of sorbed Mo to Al oxide as an outer-sphere surface complex of the MoO_4^{2-} species. Assignment of the 838 cm^{-1} band to MoO_4^{2-} was based on agreement with literature values and speciation studies, as well as the dependence of our ATR-FTIR and Raman spectra of aqueous Mo solutions as a function of pH and Mo concentration. At low pH, we observe the formation of a polymeric species in aqueous solution that is most likely $Mo_7O_{24}^{6-}$ (or protonated version of this complex). Following the rationale of Jeziorowski and Knozinger (1979), we attribute the spectra of Mo sorbed to Al oxide at low

pH to the formation of an inner-sphere surface complex that is characterized by the ATR-FTIR bands at 903 and 940 cm^{-1}. The specific identity of the surface complex (monodentate, bidentate, or "two-dimensional" polymeric surface species) is not known at this time.

Based on the assignment of the 838 cm^{-1} band to the outer-sphere MoO_4^{2-} species and the 903 and 940 cm^{-1} bands to some form of an inner-sphere surface complex, a spectroscopically derived surface complexation diagram is shown in Fig. 9.8. Although the spectra of Mo sorbed to Al oxide are similar to the spectra in solution, some important differences are apparent. Upon increasing the solution pH, the 837 and 897 cm^{-1} bands have essentially no intensity at low pH. In contrast, the spectra of Mo sorbed to Al oxide reveal that the 838 cm^{-1} band still has significant intensity at pH 4. We attribute this to the presence of some outer-sphere coordinated MoO_4^{2-}.

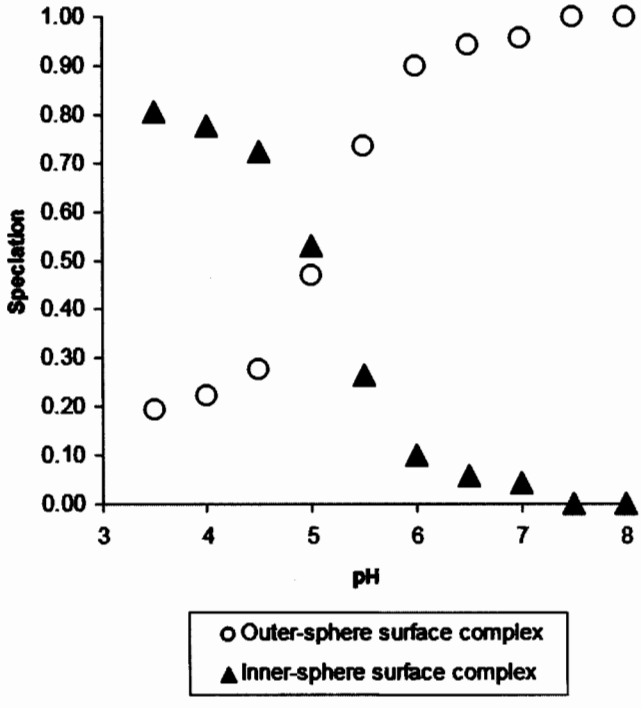

Figure 9.8: The Relative Contribution of the Outer- and Inner-Sphere Surface Complexes Sorbed to Al Oxide as a Function of pH between pH 3.5 and 8. The 837–845 cm^{-1} Band was used to Estimate the Proportion of Outer-Sphere Mo Complexed by the Surface and the Combined Intensity of the 904 and 940–947 cm^{-1} Bands were used to Estimate the Proportion of Inner-Sphere Surface Complexed Mo.

In addition, the transformation of the octahedrally coordinated Mo species to the tetrahedrally coordinated complex occurs near pH 6. This pH value is shifted to ~5 for Mo sorbed on the surface of the Al oxide. This result is most likely due to the fact that Al oxide has a positive surface charge at these pH values (<8). Thus, the local concentration of hydrogen ions [H^+_{aq}] at the interface is lower than in the bulk solution, due to the accumulation of hydroxide ions that serve to compensate for the surface charge.

To the best of our knowledge, ATR-FTIR spectra of Mo sorbed to a hydrous oxide in aqueous suspension have not been reported previously. We have shown that, in general, good agreement exists between the spectra of Mo in aqueous solution and those of Mo sorbed to Al oxide. Although a significant amount of effort has been extended to the study of Mo-based catalysts, relatively little is known about the sorption of Mo to environmentally relevant hydrous oxides in aqueous suspension.

9.3.3. Surface Complexation Modeling

The ability of the triple layer model to describe Mo adsorption on amorphous Fe oxide is depicted in Fig. 9.2a. The model described the data quantitatively below pH 6.5 and above pH 9, with deviations in the intermediate pH range. In accordance with the experimental data, the model fits do not show ionic strength dependence, despite the consideration of the outer-sphere surface complex, SOH_2^+–MoO_4^{2-}. Figure 9.2b shows triple layer model fits to Mo adsorption on amorphous Al oxide. While the model was able to fit the majority of the experimental data points, it did not show sufficient ionic strength dependence to provide a quantitative description, especially in the intermediate pH range and for the 1.0 M data. The decrease in quality of fit at 1.0 M may be due to the fact that this ionic strength is outside the applicable range of the Davies equation. The FITEQL program was unable to fit the amorphous Al oxide data using the SOH_2^+–MoO_4^{2-} surface complex. Model convergence was obtained only after replacing this species with the outer-sphere surface complex, SOH_2^+–$HMoO_4^-$.

The Mo surface speciation predicted by the triple layer model is presented in Fig. 9.9. The inner-sphere surface complex dominates at low pH and the outer-sphere surface complex predominates at high pH. This is in agreement with our Raman and ATR-FTIR spectroscopic observations and those for sulfate and selenate adsorption (Peak et al., 1999; Wijnja and Schulthess, 2000). For amorphous Al oxide, the outer-sphere surface complex dominates above pH 8, while for amorphous Fe oxide, the outer-sphere surface complex does not become predominant until pH 9.5. These results are in agreement

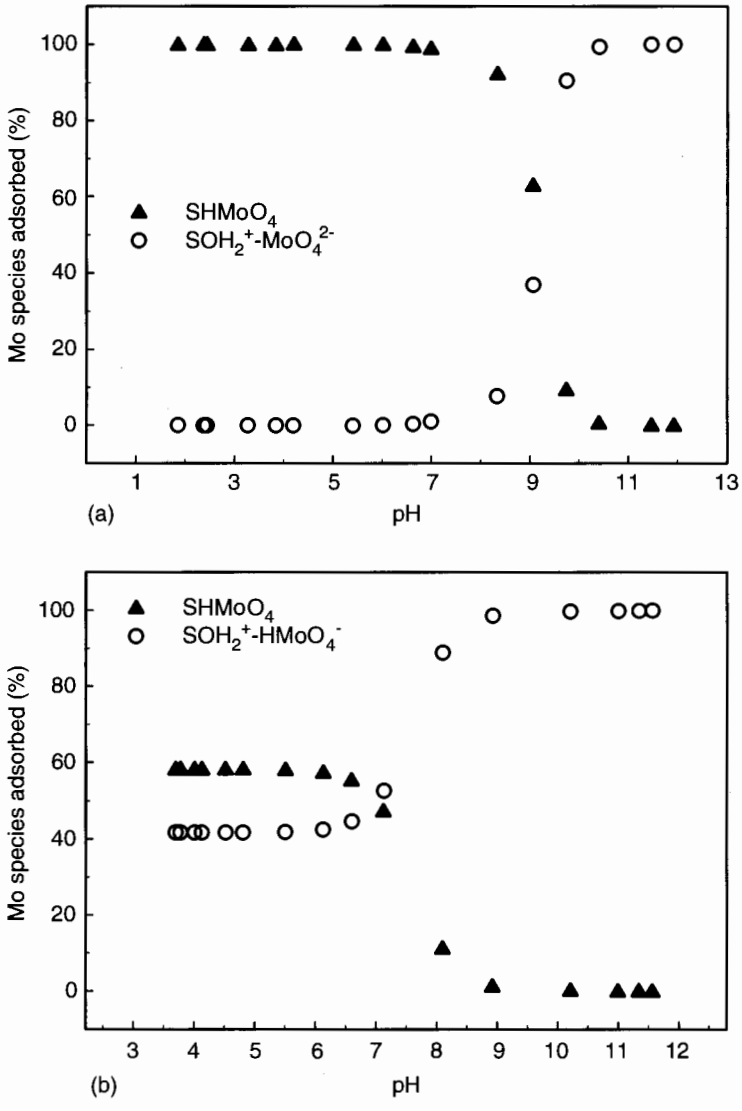

Figure 9.9: Surface Speciation Predicted by the Triple Layer Model for Mo Adsorption on: (a) Amorphous Fe Oxide; (b) Amorphous Al Oxide.

with our PZC shift observations. The crossover in dominance between inner- and outer-sphere species for the IR (pH 5) and TLM (pH 7) occur within two pH units of each other. Considering that the IR experiments were done at 100 times the Mo concentration as the adsorption experiments, the agreement is quite reasonable.

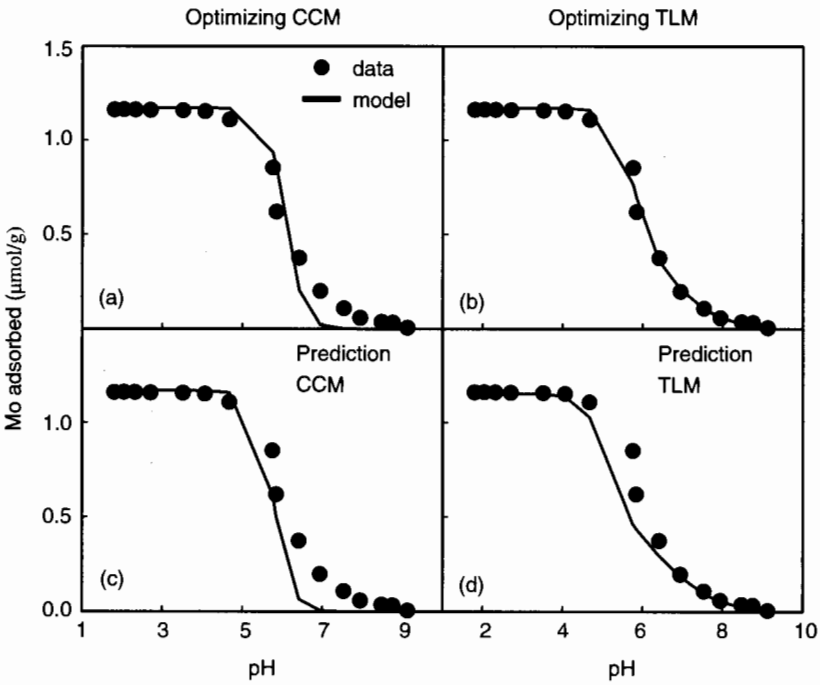

Figure 9.10: Surface Complexation Modeling of Mo Adsorption on Wyo Soil: (a) Constant Capacitance Model Monodentate Fit; (b) Triple Layer Model Inner- and Outer-Sphere Monodentate Fit; (c) Constant Capacitance Model Monodentate Prediction; (d) Triple Layer Model Inner- and Outer-Sphere Monodentate Prediction. Circles Represent Experimental Data. Model Fits are Represented by Solid Lines. Constant Capacitance Model Results from Goldberg et al. (2002).

Molybdenum adsorption as a function of solution pH had been determined previously for 36 different soil samples (Goldberg et al., 2002). Molybdenum adsorption was found to be maximal in the pH range 2–5 and to decrease rapidly with increasing pH above 5. The constant capacitance model was able to fit the Mo adsorption envelopes well on all of the soil samples, but increasing deviations occurred above pH 7.5 (see Fig. 9.10a). In an effort to improve the fit at high pH, the data were reanalyzed using the triple layer model containing one inner-sphere, $SHMoO_4$, and one outer-sphere, SOH_2^+–MoO_4^{2-}, Mo surface complexation constant. The improvement in the ability of the triple layer model approach to describe Mo adsorption on the Wyo soil is indicated in Fig. 9.10b. For reference, the original fit of the constant capacitance model to the experimental data is

presented in Fig. 9.10a. The triple layer model was able to quantitatively describe the Mo adsorption data at all pH values.

As in our previous investigation (Goldberg et al., 2002), the initial regression model was defined to be:

$$\gamma_i = \beta_0 + \beta_1(\ln \mathrm{CEC}_i) + \beta_2(\ln \mathrm{SA}_i) + \beta_3(\ln \mathrm{OC}_i) + \beta_4(\ln \mathrm{IOC}_i) + \beta_5(\ln \mathrm{Fe}_i) + \beta_6(\ln \mathrm{Al}_i) + \varepsilon_i \quad (9.19)$$

where γ represents the surface complexation constant, $\log \mathrm{K}^i_{\mathrm{Mo}}(\mathrm{int})$, β_i the empirical derived regression coefficients, and ε the residual error component, assumed to follow the usual regression modeling assumptions of normal errors. The optimization criterion used in each model building process was that the final selected prediction equation should exhibit the smallest possible jack-knifed prediction errors (Myers, 1986), on average.

Jack-knifed prediction errors (also commonly referred to as PRESS residuals) can be conveniently computed in most standard regression software packages using the relationship:

$$\hat{e}_{i,-i} = \frac{\hat{e}_i}{(1 - h_{ii})} \quad (9.20)$$

where $\hat{e}_i$ represents the ordinary prediction error, h_{ii} the ith diagonal element of the regression model projection matrix, and $\hat{e}_{i,-i}$ the prediction error one obtains if the ith observation is not included in the model estimation process. Jack-knifing essentially represents a "one-at-a-time" deletion and re-estimation technique and is commonly used to develop robust, regression-based prediction models (Myers, 1986). The PRESS statistic is defined to be the sum of the squared $\hat{e}_{i,-i}$ components and the jack-knifed mean square error (MSE) is simply defined to be the value of the PRESS statistic divided by the sample size.

Model optimization was carried out using a backwards elimination, BWE, procedure, where the critical cut-off value used for parameter removal was set to $\alpha = 0.15$ (Myers, 1986). Based on the results from this BWE procedure, a reduced prediction equation was specified for each surface complexation constant. During the BWE procedure, the PRESS statistic was calculated after each parameter elimination step to verify that this statistic was consistently reduced. Upon termination of the BWE procedure, the remaining parameters left in the reduced prediction equations where then individually deleted and the PRESS statistic was recalculated. This last step was performed in order to verify that the BWE procedure had indeed also minimized the jack-knifed prediction variance. All regression model analyses were performed using the SAS REG procedure (SAS, 1999).

For the inner-sphere surface complexation constant, the initial estimate of Eq. (9.19) produced an R^2 value of 0.486 and a jack-knifed MSE estimate of 0.519. An application of the BWE procedure removed all variables except lnIOC and lnAl; the corresponding R^2 and jack-knifed MSE for this reduced model were 0.472 and 0.382, respectively. The PRESS statistic increased when either of these two remaining regression variables was removed. Hence, the final estimated prediction equation for $\log K^{is}_{Mo}(int)$ was defined to be:

$$\log K^{is}_{Mo}(int) = \beta_0 + \beta_1(\ln IOC) + \beta_2(\ln Al) + \varepsilon \tag{9.21}$$

The corresponding parameter estimates for this model are shown in Table 9.1. The specific predicted and jack-knife predicted $\log K^{is}_{Mo}(int)$ constants for the soil samples are shown in Table 9.2.

For the outer-sphere surface complexation constant, the initial estimate of Eq. (9.19) produced a slightly higher R^2 value of 0.524 and a jack-knifed MSE estimate of 0.098. An application of the BWE procedure removed the lnIOC, lnAl, and lnSA regression variables; the corresponding R^2 and jack-knifed MSE for this reduced model were 0.487 and 0.080, respectively. Once again, the PRESS statistic increased when each of the three remaining regression variables were removed. Therefore, the final estimated prediction equation for $\log K^{2os}_{Mo}(int)$ was defined to be:

$$\log K^{2os}_{Mo}(int) = \beta_0 + \beta_1(\ln CEC) + \beta_2(\ln OC) + \beta_3(\ln Fe) + \varepsilon \tag{9.22}$$

The corresponding parameter estimates for this model are shown in Table 9.1, and the specific predicted and jack-knife predicted $\log K^{2os}_{Mo}(int)$ constants for the soil samples are shown in Table 9.2.

Table 9.1: Regression Model Parameter Estimates and Standard Errors for the Triple Layer Model Surface Complexation Model Prediction Equations.

Parameter	Estimate	Standard error	*t*-score	Prob > |*t*|
$\log K^{is}_{Mo}$ (int) parameter estimates				
Intercept	5.565	0.503	11.07	<0.0001
ln(IOC)	0.171	0.039	4.36	0.0002
ln(Fe)	0.373	0.172	2.17	0.0390
$\log K^{2os}_{Mo}$ (int) parameter estimates				
Intercept	1.672	0.448	3.74	0.0009
ln(CEC)	−0.412	0.088	−4.70	<0.0001
ln(OC)	0.131	0.068	1.92	0.0654
ln(Fe)	0.178	0.079	2.26	0.0326

Table 9.2: Triple Layer Model Surface Complexation Constants Obtained by Optimization and from the Prediction Equations.

Soil	Fitted Log K^{is}_{Mo}	Fitted Log K^{2os}_{Mo}	Predicted Log K^{is}_{Mo}	Predicted Log K^{2os}_{Mo}	Jack-knife predicted Log K^{is}_{Mo}	Jack-knife predicted Log K^{2os}_{Mo}
Altamont	4.01	−0.518	3.90	−0.332	3.90	−0.303
	2.81	−0.496	3.32	−0.449	3.37	−0.447
	2.70	−0.553	3.37	−0.506	3.44	−0.503
Arlington	3.95	−0.456	3.83	−0.386	3.83	−0.383
Avon	4.09	−0.158	3.79	−0.477	3.78	−0.528
Bonsall	3.19	−0.166	3.66	−0.077	3.69	−0.065
Chino	4.30	−1.126	4.81	−0.881	4.91	−0.825
Diablo	3.56	−0.903	4.09	−0.650	4.12	−0.626
	3.54	−0.805	4.38	−0.536	4.43	−0.504
Fallbrook	3.10	−0.159	3.48	−0.402	3.55	−0.421
Fiander	4.31	−0.718	4.66	−0.733	4.70	−0.736
Haines	4.70	−0.411	4.14	−0.396	3.95	−0.392
Hanford	5.14	0.087	4.31	−0.024	4.20	−0.265
Hesperia	3.07	−0.391	3.22	−0.192	3.24	−0.164
Holtville	4.29	−0.269	4.30	−0.331	4.30	−0.338
Imperial	4.38	−0.550	4.57	−0.674	4.59	−0.689
Lost Hills	5.07	−0.064	4.20	−0.777	4.15	−0.933
Nohili	5.73	−0.251	4.97	−0.478	4.59	−0.641
Pachappa	4.73	−0.978	4.23	−0.545	4.21	−0.508
	3.16	0.319	3.54	−0.012	3.56	−0.067
	3.14	0.102	3.54	−0.012	3.56	−0.031
	3.95	−0.166	3.19	−0.302	3.10	−0.335
Porterville	3.27	−0.514	3.72	−0.513	3.75	−0.513
	4.07	−0.750	3.72	−0.513	3.69	−0.496
Reagan	3.84	−0.241	4.51	−0.353	4.61	−0.360
Ryepatch	4.29	−0.905	4.44	−0.866	4.45	−0.853
Sebree	3.79	−0.354	3.16	0.026	3.08	0.115
Wasco	2.79	−0.641	3.18	−0.437	3.23	−0.408
Wyo	4.72	−0.274	3.54	−0.324	3.42	−0.330
Yolo	4.25	−0.388	4.16	−0.362	4.15	−0.359

Equations (9.21) and (9.22) were each derived independently, using the same initial set of optimized surface complexation constants. The jack-knifed prediction columns show the ability of the model to predict each individual soil surface complexation constant, without using this constant in the fitting process. The general excellent agreement between the predicted surface

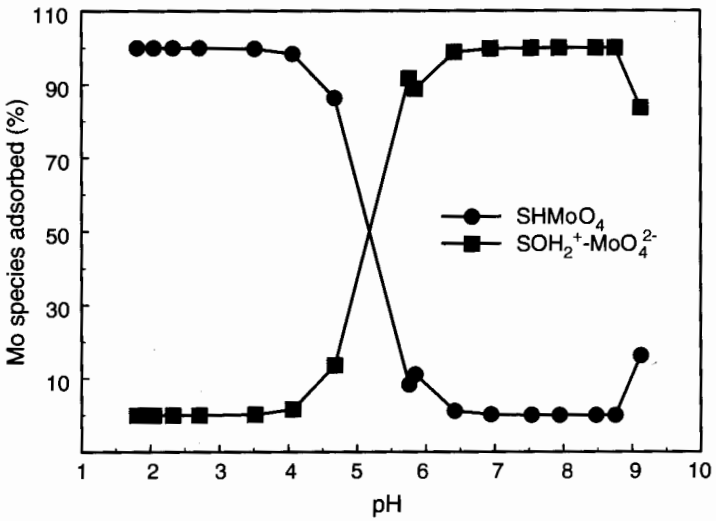

Figure 9.11: Surface Speciation Predicted by the Triple Layer Model for Mo Adsorption on Wyo Soil.

complexation constants and the jack-knife estimates suggests that the regression prediction equations for both surface complexation constants should have good predictive capability.

Figure 9.10d presents the ability of the triple layer model to predict Mo adsorption from chemical properties for one of the soils predicted previously using the constant capacitance model (Goldberg et al., 2002). While the prediction (Fig. 9.10d) is, of course, less good than the result of the model optimization (Fig. 9.10b), it is at least semi-quantitative at all pH values. The tremendous improvement in the quality of the triple layer model prediction at pH values above 7 (Fig. 9.10d) over the constant capacitance model prediction (Fig. 9.10c) is especially significant for prediction of Mo adsorption in arid zone soils where Mo can accumulate in forage plants to levels detrimental to the health of grazing ruminant animals. The surface speciation predicted for the Wyo soil is presented in Fig. 9.11. The outer-sphere Mo surface complex is predicted to dominate above pH 6. This is in agreement with the surface speciation predicted from spectroscopy for Mo adsorption on amorphous Al oxide.

9.4. Conclusions

The results of all experimental methods, both macroscopic (PZC shifts and ionic strength effects) and microscopic (Raman and ATR-FTIR

spectroscopies), provide self-consistent mechanisms for Mo adsorption on amorphous oxides. Molybdate forms predominantly inner-sphere surface complexes on both oxides at low pH and outer-sphere surface complexes dominate at high pH. The inner-sphere surface complex predominates to a greater extent for Mo adsorption on amorphous Fe oxide, while the outer-sphere surface complex is more significant for Mo adsorption on amorphous Al oxide. The triple layer model containing both an inner-sphere and an outer-sphere surface complex was able to describe and predict Mo adsorption on a large group of soils at all pH values investigated. The predominance diagram for the Mo surface species in soil was in complete agreement with that obtained spectroscopically for Mo adsorption on amorphous Al oxide.

ACKNOWLEDGMENTS

Gratitude is expressed to Mr. H.S. Forster and Mr. G.S. Premachandra for technical assistance.

REFERENCES

Bare, W. D., Souter, P. F., & Andrews, L. (1998). Reactions of laser-ablated molybdenum and tungsten atoms with dioxygen. Resolved infrared spectra of natural molybdenum and tungsten isotopic oxides in argon matrices. *J. Phys. Chem. A*, **102**, 8279–8286.

Bibak, A., & Borggaard, O. K. (1994). Molybdenum adsorption by aluminum and iron oxides and humic acid. *Soil Sci.*, **158**, 323–327.

Bourikas, K., Hiemstra, T., & van Riemsdijk, W. H. (2001). Adsorption of molybdate monomers and polymers on titania with a multisite approach. *J. Phys. Chem. B*, **105**, 2393–2403.

Coffin, D. E. (1963). A method for the determination of free iron oxide in soils and clays. *Can. J. Soil Sci.*, **43**, 7–17.

Davis, J. A., & Kent, D. B. (1990). Surface complexation modeling in aqueous geochemistry. *Rev. Mineral.*, **23**, 117–260.

Dzombak, D. A., & Morel, F. M. M. (1990). *Surface Complexation Modeling. Hydrous Ferric Oxide*. Wiley, New York.

El Shafei, G. M. S., Moussa, N. A., & Philip, C. A. (2000). Association of molybdenum ionic species with alumina surface. *J. Colloid Interface Sci.*, **228**, 105–113.

Farmer, V. C. (1974). The layer silicates. In: V. C. Farmer (Ed). *The Infrared Spectra of Minerals*. Mineral Society, London, pp. 331–359.

Ferreiro, E. A., Helmy, A. K., & de Bussetti, S. G. (1985). Molybdate sorption by oxides of aluminium and iron. *Z. Pflanzenernaehr. Bodenkd.*, **148**, 559–566.

Goldberg, S. (1992). Use of surface complexation models in soil chemical systems. *Adv. Agron.*, **47**, 233–329.

Goldberg, S. (2002). Competitive adsorption of arsenate and arsenite on oxides and clay minerals. *Soil Sci. Soc. Am. J.*, **66**, 413–421.

Goldberg, S., & Forster, H. S. (1998). Factors affecting molybdenum adsorption by soils and minerals. *Soil Sci.*, **163**, 109–114.

Goldberg, S., Forster, H. S., & Godfrey, C. L. (1996). Molybdenum adsorption on oxides, clay minerals, and soils. *Soil Sci. Soc. Am. J.*, **60**, 425–432.

Goldberg, S., & Johnston, C. T. (2001). Mechanisms of arsenic adsorption on amorphous oxides evaluated using macroscopic measurements, vibrational spectroscopy, and surface complexation modeling. *J. Colloid Interface Sci.*, **234**, 204–216.

Goldberg, S., Lesch, S. M., & Suarez, D. L. (2002). Predicting molybdenum adsorption by soils using soil chemical parameters in the constant capacitance model. *Soil Sci. Soc. Am. J.*, **66**, 1836–1842.

Goldberg, S., Su, C., & Forster, H. S. (1998). Sorption of molybdenum on oxides, clay minerals, and soils: Mechanisms and models. In: E. A. Jenne (Ed). *Adsorption of Metals by Geomedia: Variables, Mechanisms, and Model Applications.* Proc. Am. Chem. Soc. Symp., Academic Press, San Diego, CA, pp. 401–426.

Gonzalez, B. R., Appelt, H., Schalscha, E. B., & Bingham, F. T. (1974). Molybdate adsorption characteristics of volcanic-ash-derived soils in Chile. *Soil Sci. Soc. Am. Proc.*, **38**, 903–906.

Gustafsson, J. P. (2003). Modelling molybdate and tungstate adsorption to ferrihydrite. *Chem. Geol.*, **200**, 105–115.

Hayes, K. F., Papelis, C., & Leckie, J. O. (1988). Modeling ionic strength effects on anion adsorption at hydrous oxide/solution interfaces. *J. Colloid Interface Sci.*, **125**, 717–726.

Herbelin, A. L., & Westall, J. C. (1996). *FITEQL: A Computer Program for Determination of Chemical Equilibrium Constants from Experimental Data.* Rep. 96–01, Version 3.2, Department of Chemistry, Oregon State University, Corvallis, OR.

Herzberg, G. (1945). *Molecular Spectra and Molecular Structure: II. Infrared and Raman Spectra of Polyatomic Molecules.* Van Nostrand Reinhold Company, New York.

Jeziorowski, H., & Knozinger, H. (1979). Raman and ultraviolet spectroscopic characterization of molybdena on alumina catalysts. *J. Phys. Chem.*, **83**, 1166–1173.

Johnston, C. T., & Aochi, Y. O. (1996). Fourier transform infrared and Raman spectroscopy. In: D. L. Sparks et al. (Eds). *Methods of Soil Analysis: Part 3. Chemical Methods.* Soil Science Society of America, Madison, WI.

Johnston, C. T., & Wang, S. L. (2002). Application of vibrational spectroscopy in soil and environmental sciences. In: J. M. Chalmers, & P. R. Griffiths (Eds). *Handbook of Vibrational Spectroscopy.* Wiley, New York.

Jones, L. H. P. (1957). The solubility of molybdenum in simplified systems and aqueous soil suspensions. *J. Soil Sci.*, **8**, 313–327.

Knozinger, H., & Jeziorowski, H. (1978). Raman-spectra of molybdenum oxide supported on surface of aluminas. *J. Phys. Chem.*, **82**, 2002–2005.

Kyriacou, D. (1967). The pH-dependence of adsorption of metallic oxyanions by ferric oxide powder. *Surf. Sci.*, **8**, 370–372.

Lang, F., & Kaupenjohann, M. (1999). Molybdenum fractions and mobilization kinetics in acid forest soils. *J. Plant Nutr. Soil Sci.*, **162**, 309–314.

Lang, F., & Kaupenjohann, M. (2003). Immobilisation of molybdate by iron oxides: Effects of organic coatings. *Geoderma*, **113**, 31–46.

Lang, F., Pohlmeier, A., & Kaupenjohann, M. (2000). Mechanism of molybdenum sorption to iron oxides using pressure-jump relaxation. *J. Plant Nutr. Soil Sci.*, **163**, 571–575.

Lefevre, G., & Fedoroff, M. (2006). In situ Fourier-transform infrared spectroscopy studies of inorganic ions adsorption on metal oxides and hydroxides. *Adv. Colloid Interface Sci.*, **107**, 109–123.

Long, D. A. (1977). *Raman Spectroscopy*. McGraw-Hill, New York.

McBride, M. B. (1997). A critique of diffuse double layer models applied to colloid and surface chemistry. *Clays Clay Miner.*, **45**, 598–608.

McKenzie, R. M. (1983). The adsorption of molybdenum on oxide surfaces. *Aust. J. Soil Res.*, **21**, 505–513.

McLaughlin, J. R., Ryden, J. C., & Syers, J. K. (1981). Sorption of inorganic phosphate by iron and aluminium-containing components. *J. Soil Sci.*, **32**, 365–377.

Mikkonen, A., & Tummavuori, J. (1993). Retention of molybdenum (VI) by three Finnish mineral soils. *Acta Agric. Scand. B Soil Plant Sci.*, **43**, 206–212.

Motta, M. M., & Miranda, C. F. (1989). Molybdate adsorption on kaolinite, montmorillonite, and illite: Constant capacitance modeling. *Soil Sci. Soc. Am. J.*, **53**, 380–385.

Murphy, L. S., & Walsh, L. M. (1972). Correction of micronutrient deficiencies with fertilizers. In: J. J. Mortvedt, P. M. Giordano, & W. L. Lindsay (Eds). *Micronutrients in Agriculture*. Soil Science Society of America, Madison, WI, pp. 347–387.

Myers, R. H. (1986). *Classical and Modern Regression with Applications*. Duxbury Press, Boston, MA.

O'Connor, G. A., Brobst, R. B., Chaney, R. L., Kincaid, R. L., McDowell, L. R., Pierzynski, G. M., Rubin, A., & Van Riper, G. G. (2001). A modified risk assessment to establish molybdenum standards for land application of biosolids. *J. Environ. Qual.*, **30**, 1490–1507.

Peak, D., Ford, R. G., & Sparks, D. L. (1999). An in situ ATR-FTIR investigation of sulfate bonding mechanisms on goethite. *J. Colloid Interface Sci.*, **218**, 289–299.

Reisenauer, H. M., Tabikh, A. A., & Stout, P. R. (1962). Molybdenum reactions with soils and the hydrous oxides of iron, aluminum, and titanium. *Soil Sci. Soc. Am. J.*, **26**, 23–37.

Reisenauer, H. M., Walsh, L. M., & Hoeft, R. G. (1973). Testing soils for sulphur, boron, molybdenum, and chlorine. In: L. M. Walsh, & J. D. Beaton (Eds). *Soil*

Testing and Plant Analysis. Revised Edition. Soil Science Society of America, Madison, WI, pp. 173–200.

Reyes, E. D., & Jurinak, J. J. (1967). A mechanism of molybdate adsorption on αFe_2O_3. *Soil Sci. Soc. Am. J.*, **31**, 637–641.

Saripalli, P. K., McGrail, B. P., & Girvin, D. C. (2002). Adsorption of molybdenum on to anatase from dilute aqueous solutions. *Appl. Geochem.*, **17**, 649–656.

SAS (1999). *SAS/STAT Users Guide.* Version 8. SAS Institute Inc., Cary, NC.

Sims, J. T., & Bingham, F. T. (1968). Retention of boron by layer silicates, sesquioxides, and soil materials: II. Sesquioxides. *Soil Sci. Soc. Am. Proc.*, **32**, 364–369.

Spanos, N., & Lycourghiotis, A. (1995). Codeposition of $Mo^{(VI)}$ species and Ni^{2+} ions on the γ-alumina surface: Mechanistic model. *J. Colloid Interface Sci.*, **171**, 306–318.

Spanos, N., Vordonis, L., Kordulis, C. H., Koutsoukos, P. G., & Lycourghiotis, A. (1990a). Molybdenum-oxo species deposited on alumina by adsorption. II. Regulation of the surface Mo^{VI} concentration by control of the protonated surface hydroxyls. *J. Catal.*, **124**, 315–323.

Spanos, N., Vordonis, L., Kordulis, C. H., & Lycourghiotis, A. (1990b). Molybdenum-oxo species deposited on alumina by adsorption. I. Mechanism of the adsorption. *J. Catal.*, **124**, 301–314.

Sposito, G. (1983). Foundations of surface complexation models of the oxide–aqueous solution interface. *J. Colloid Interface Sci.*, **91**, 329–340.

Sprycha, R. (1989a). Electrical double layer at alumina/electrolyte interface. I. Surface charge and zeta potential. *J. Colloid Interface Sci.*, **127**, 1–11.

Sprycha, R. (1989b). Electrical double layer at alumina/electrolyte interface. II. Adsorption of supporting electrolyte ions. *J. Colloid Interface Sci.*, **127**, 12–25.

Stollenwerk, K. G. (1995). Modeling the effects of variable groundwater chemistry on adsorption of molybdate. *Water Resour. Res.*, **31**, 347–357.

Su, C., & Suarez, D. L. (1997). In situ infrared speciation of adsorbed carbonate on aluminum and iron oxides. *Clays Clay Miner.*, **45**, 814–825.

Tossell, J. A. (2005). Calculating the partitioning of the isotopes of Mo between oxidic and sulfidic species in aqueous solution. *Geochim. Cosmochim. Acta*, **69**, A210.

Vissenberg, M. J., Joosten, L. J. M., Heffels, M. M. E. H., van Welsenes, A. J., de Beer, V. H. J., van Santen, R. A., & van Veen, J. A. R. (2000). Tungstate versus molybdate adsorption on oxidic surfaces: A chemical approach. *J. Phys. Chem. B*, **104**, 8456–8461.

Vordonis, L., Koutsoukos, P. G., & Lycourghiotis, A. (1990). Adsorption of molybdates on doped γ-aluminas in alkaline solutions. *Colloids Surf.*, **50**, 353–361.

Wang, S. L., & Johnston, C. T. (2000). Assignment of the structural OH stretching bands of gibbsite. *Am. Mineral.*, **85**, 739–744.

Wang, X. F., & Andrews, L. (2006). Contrasting products in the reactions of Cr, Mo, and W atoms with H_2O_2: Argon matrix infrared spectra and theoretical calculations. *J. Phys. Chem. A*, **110**, 10409–10418.

Weinstock, N., Schulze, H., & Muller, A. (1973). Assignment of ν_2 (E) and ν_4 (F_2) of tetrahedral species by calculation of the relative Raman intensities: The vibrational spectra of VO_4^{3-}, CrO_4^{2-}, MoO_4^{2-}, WO_4^{2-}, MnO_4^-, TcO_4^-, ReO_4^-, RuO_4, and OsO_4. *J. Chem. Phys.*, **59**, 5063–5067.

Wijnja, H., & Schulthess, C. P. (2000). Vibrational spectroscopy of selenate and sulfate adsorption mechanisms on Fe and Al (hydr)oxide surfaces. *J. Colloid Interface Sci.*, **229**, 286–297.

Wu, C.-H., Lo, S.-L., Lin, C.-F., & Kuo, C.-Y. (2001). Modeling competitive adsorption of molybdate, sulfate, and selenate on γ-Al_2O_3 by the triple-layer model. *J. Colloid Interface Sci.*, **233**, 259–264.

Xu, N., Christodoulatos, C., & Braida, W. (2006a). Adsorption of molybdate and tetrathiomolybdate onto pyrite and goethite: Effect of pH and competitive anions. *Chemosphere*, **62**, 1726–1735.

Xu, N., Christodoulatos, C., & Braida, W. (2006b). Modeling the competitive effect of phosphate, sulfate, silicate, and tungstate anions on the adsorption of molybdate onto goethite. *Chemosphere*, **64**, 1325–1333.

Zhang, P., & Sparks, D. L. (1989). Kinetics and mechanisms of molybdate adsorption/desorption at the goethite/water interface using pressure-jump relaxation. *Soil Sci. Soc. Am. J.*, **53**, 1028–1034.

Zhang, P., & Sparks, D. L. (1990). Kinetics of selenate and selenite adsorption/desorption at the goethite/water interface. *Environ. Sci. Technol.*, **24**, 1848–1856.